Available online at www.sciencedirect.com
SCIENCE DIRECT
Journal of Catalysis 230 (2005) 327–338
JOURNAL OF CATALYSIS
www.elsevier.com/locate/jcat

Synthesis of acidic Al-MCM-48: influence of the Si/Al ratio, degree of the surfactant hydroxyl exchange, and post-treatment in NH_4F solution

J.M. Campelo [a,*], D. Luna [a], R. Luque [a], J.M. Marinas [a], A.A. Romero [a], J.J. Calvino [b], M.P. Rodríguez-Luque [b]

[a] *Departamento de Química Orgánica, Facultad de Ciencias, Universidad de Córdoba, Campus Universitario de Rabanales, Edificio Marie Curie (C3), E-14014 Córdoba, Spain*
[b] *Departamento de Ciencia de los Materiales e Ingeniería Metalúrgica y Química Inorgánica, Universidad de Cádiz, Polígono Río San Pedro, s/n, Apdo. 40, 11510 Puerto Real, Cádiz, Spain*

Received 4 October 2004; revised 5 December 2004; accepted 6 December 2004

Available online 25 January 2005

Abstract

Al-MCM-48 mesostructures with different Al contents (Si/Al = 40, 30, and 20) have been prepared with hydroxyl-exchanged cetyltrimethylammonium bromide as the template and a post-synthesis treatment in NH_4F solution. The solid structures were analyzed by XRD, N_2 adsorption, DRIFT, SEM, HREM, and ^{27}Al and ^{29}Si MAS NMR. Moreover, surface acidity was determined with the use of pyridine (Py) and 2,6-dimethylpyridine (DMPy) as probe molecules. The catalytic activity of Al-MCM-48 materials in isopropylbenzene dealkylation was compared with those of the microporous H-Y and ZSM-5 zeolites and that of a commercial silica–alumina catalyst (Harshaw, Si235, 13 wt% alumina). For these solids, the catalytic activity was related to the tetrahedral or octahedral (probably AlO_5F species) aluminum for nonfluorinated and fluorinated catalysts, respectively.

Keywords: Heterogeneous catalysis; Mesoporous materials; MCM-48

1. Introduction

The importance of M41S materials in size- and shape-selective applications is well known, because they are promising catalysts for acid-catalyzed reactions in the petrochemistry industry for the manufacture of fuels, petrochemicals, and fine chemicals [1]. This M41S family of mesoporous molecular sieves has been classified into three subgroups: a hexagonal phase, referred to as MCM-41, with an one-dimensional pore system; a cubic phase known as MCM-48, with a three-dimensional pore system; and an unstable lamellar phase (MCM-50). These materials feature a combination of important properties, including a well-defined pore size, which can be tailored in the range of 16–100 Å; long-range ordering; high thermal stability; and potential ability for isomorphous substitution. The improvement in structural and hydrothermal stability and in the acidity of mesostructured MCM-48 materials has become a major challenge in the last few years [2–13]. Some of the approaches that have been proposed to enhance the structural and hydrothermal stability of MCM-48 materials are post-synthesis restructuring in salt solution [2,5], HF addition [3], post-synthesis hydrothermal treatment [4], direct addition of NaF [5], and post-synthesis treatment in water [10]. In contrast, little is known about the acidity and catalytic activity in the MCM-48 cubic phase [11–13].

Nevertheless, quite a bit of information is available on the synthesis and characterization of the mesoporous molecular sieve MCM-48 [14–25]. However, to obtain the acidic mesoporous Al-MCM-48 catalyst, transformation into the NH_4 form through ammonium ion exchange followed by thermal treatment at high temperatures is necessary and results in the H-Al-MCM-48 form [11–13]. Therefore, both the weak and

* Corresponding author.
E-mail address: qo1capej@uco.es (J.M. Campelo).

0021-9517/$ – see front matter
doi:10.1016/j.jcat.2004.12.004

medium-strength acid sites present in MCM-48, the lack of hydrothermal stability, and the difficulties entailed in achieving direct acid catalysts (without ion exchange) would limit the successful application of these materials in acid catalysis.

On the other hand, in previous studies of M41S materials, fluorination improved the structural and hydrothermal stability [3,5] and the acidity and catalytic activity [26] of these materials. Here we report on a reproducible method that uses hydroxyl-exchanged cetyl-trimethylammonium bromide to synthesize Al-MCM-48 (Si/Al ratios ranging from 40 to 20) with increased acidity and catalytic activity, and on its post-synthesis treatment of samples with a NH_4F solution to improve the quality and acidity of the Al-MCM-48 structures.

Samples were synthesized and characterized by X-ray diffraction (XRD), N_2 adsorption, diffuse reflectance infrared Fourier transform (DRIFT), scanning electron microscopy (SEM), high-resolution electron microscopy (HREM), and ^{27}Al and ^{29}Si magic-angle spinning solid-state nuclear magnetic resonance (MAS NMR) analysis. Studies were made of the effect of the Si/Al ratio, the degree of surfactant hydroxyl exchange, and the post-synthesis treatment in NH_4F solution on phase transformation in mesoporous materials. Moreover, surface acidity was measured with the use of pyridine (Py) and 2,6-dimethylpyridine (DMPy) as probe molecules. The vapor-phase isopropylbenzene conversion was studied as a catalytic test as well, and activities of samples were compared with those of microporous H-Y and ZSM-5 zeolites and with that of a commercial silica–alumina catalyst (Si235, 13 wt% alumina).

2. Experimental

2.1. Synthesis procedure

Tetraethyl orthosilicate (TEOS) and $AlCl_3 \cdot 6H_2O$ were used as Si and Al sources, respectively, and cetyl-trimethylammonium bromide (CTMABr) was the template, with a degree of exchange of hydroxide for bromide ion of 50 and 40%, respectively, with the Ambersep 900-OH ion exchange resin (Acros). Al-MCM-48 samples were prepared by two procedures: (i) They were synthesized at room temperature, according to the procedure described by Grün et al. [27], with some variations. First of all, CTMABr/OH was added instead of pure CTMABr. The surfactant–silica molar ratio in the gel mixture was 0.3, and the reaction time was reduced to 20 min before final filtration of the mixture. (ii) The as-synthesized samples obtained in (i) were suspended in 300 ml of NH_4F 0.1 M for 34 h. The product thus obtained was filtered, dried at 298 K, and calcined at 823 K in air for 24 h.

Samples were denoted XAl-Y or XAl-Y-F, where F refers to NH_4F post-treatment, X = 40, 30, 20, and 15 is the Si/Al ratio in the synthesis gel, and Y = 50 and 40 is the degree of exchange (mol%) of hydroxide for bromide ion. In addition, for comparative purposes, the Al-41-30 (MCM-41 structure, Si/Al = 30) sample was synthesized with exactly the same procedure as described by Grün et al. [27]. Finally, we unsuccessfully tried to synthesize the Al-MCM-48 mesophase described by Schumacher et al. [17].

2.2. Characterization

Powder X-ray diffraction patterns were carried out with a Siemens D-5000 diffractometer with Cu-K_α ($\lambda = 1.518$ Å), a step size of 0.02°, and a counting time per step of 1.2 s, over a range of 2° to 10°.

Nitrogen physisorption was measured with an ASAP 2000 Micromeritics instrument model at 77 K. The samples were first outgassed at 473 K for 24 h. The linear part of the Brunauer–Emmett–Teller (BET) equation (relative pressure between 0.05 and 0.22) was used for the specific surface area determination. Pore size distribution (PSD) was calculated with the use of the adsorption branch of the N_2 physisorption isotherms and the Barret–Joyner–Halenda (BJH) formula [28]. The cumulative pore volume (V_{BJH}) of the mesopores was obtained from the PSD curve.

Scanning electron micrographs were recorded with a JEOL JSM-6300 scanning microscope, and the elemental composition of the calcined samples was assessed by energy-dispersive X-ray analysis (EDX) at 20 kV. The Si/Al molar ratios of calcined MCM-48 are in close agreement with the composition of the gel mixtures (Table 1).

HREM images were recorded in a JEOL2000-EX microscope operating at an accelerating voltage of 200 kV. The structural resolution of this microscope is 0.21 nm. The electron microscopy specimens were prepared by two different procedures: (1) The particles of the samples to be investigated were deposited directly on 3-mm holey carbon-coated copper grids. We achieved this by dipping the grid directly into the powder of the samples, to avoid contact with any solvent, and then blowing off the excess powder. (2) Ultrathin sections of the samples were prepared with an ultramicrotome. In this case the samples were previously embedded in an epoxy resin. Sections with a thickness of 20–40 nm were finally obtained and mounted on 3-mm holey carbon copper grids.

HREM images were digitized from negative plates with a KAPPA DX2 CCD camera (1380 × 1028, 16 bit). Image analysis was performed on digitized images with Digital Micrograph 3.4.3. The digital diffraction patterns (DDPs) shown here correspond to the log-scaled power spectrum of the corresponding fast Fourier transforms (FFTs).

Thermal analysis was performed by simultaneous thermal gravimetric and differential thermal analysis (ATG-DTA) measurement with a Setsys 12 Setaram thermobalance. Samples were heated in air (50 ml/min) in a temperature range of 293–1173 K at a heating rate of 10 K min^{-1}.

Temperature-programmed mass spectrometry (TP-MS) experiments were carried out in an on-line device with a VG GAS Prolab quadrupole mass spectrometer. This de-

Table 1
Structural and textural properties and composition of Al-M41S calcined samples

Sample	Structure	$d_{(211)}$ (Å)	$d_{(100)}$ (Å)	a_0[a] (Å)	D_{BJH} (Å)	V_{BJH} ($cm^3\,g^{-1}$)	S_{BET} ($m^2\,g^{-1}$)	C_{BET} ($m^2\,g^{-1}$)	ε[b] (Å)	Si/Al EDX
40Al-50	Cubic	32	–	79	19	0.42	1469	29	16	50
30Al-50	Cubic	33	–	82	18	0.28	1328	38	17	37
20Al-50	Cubic	31	–	76	18	0.28	1419	28	16	24
15Al-50	Hexagonal	–	33	38	18	0.30	1351	25	20	20
40Al-50-F	Cubic	35	–	86	21	0.86	1086	51	17	40
30Al-50-F	Cubic	35	–	87	22	0.87	1036	51	17	33
20Al-50-F	Cubic	32	–	77	21	0.80	1070	44	15	20
15Al-50-F	Hexagonal	–	33	38	22	0.68	912	54	16	15
40Al-40	Cubic	33	–	81	19	0.45	1309	38	17	37
30Al-40	Hexagonal	–	33	38	19	0.40	1305	33	19	36
20Al-40	Hexagonal	–	35	40	21	0.75	1161	44	19	24
15Al-40	Hexagonal	–	35	40	21	0.67	991	50	19	20
40Al-40-F	Cubic	35	–	85	21	0.75	1042	48	17	44
30Al-40-F	Hexagonal	–	34	39	20	0.69	1054	49	19	32
20Al-40-F	Hexagonal	–	34	40	21	0.65	1016	54	19	22
15Al-40-F	Hexagonal	–	35	41	21	0.59	970	51	20	16
Al-41-30	Hexagonal	–	34	39	22	0.77	1179	48	17	32

[a] Cubic and hexagonal unit cell calculated as $a_0 = d_{211}\sqrt{6}$ and $a_0 = 2d_{100}/\sqrt{3}$, respectively.
[b] Wall thickness of cubic and hexagonal structure calculated as $\varepsilon = (a_0/3.092) - (D_{BJH}/2)$ and $\varepsilon = a_0 - D_{BJH}$, respectively.

vice consisted of a microcatalytic reactor with an on-line MS detector and an open-air connection. The reactor was a vertically mounted 80-mm-long stainless-steel tube with an inside diameter of 4 mm. The as-made sample (ca. 40 mg) was placed between two layers of quartz wool. The vertical reactor was surrounded by a well-insulated jacked heater. As in ATG-DTA, the experimental conditions were as follows: heating rate, 10 K/min, in the temperature range 323–873 K; flow rate (air), 50 ml/min. The mass spectrometer was operated in the multiple ion monitoring (MIM) mode.

^{27}Al (pulse 1 μs; recycle delay: 0.3 s) and ^{29}Si (pulse: 6 μs; recycle delay: 600 s) MAS NMR spectra were recorded on a Bruker ACP-400 multinuclear spectrometer at 104.26 and 79.45 MHz, respectively. The chemical shifts are given in ppm from $Al(H_2O)_6^{3+}$ and tetramethylsilane as external standard references for Al and Si, respectively.

DRIFT spectra were recorded on a Bomem MB series instrument equipped with an "environmental chamber" (Spectra Tech, P/N 0030-100) placed in the diffuse reflectance attachment (Spectra Tech, Collector). The resolution was 8 cm^{-1}, and 256 scans were averaged to obtain spectra in the 4000–400 cm^{-1} range. Single-beam spectra were measured with the spectra of KBr or of as-synthesized Al-MCM-48 acquired at the same temperature as the sample. Calcined samples were dried at 423 K for 24 h, mixed with KBr to 15 wt%, placed in an environmental chamber cell with a 20 ml min^{-1} flow of nitrogen, heated to 573 K, and held at this temperature for 1 h before spectrum measurement.

2.3. Surface acidity

Surface acidity was measured in a dynamic mode with a previously described pulse chromatographic technique involving gas-phase (573 K) adsorption of Py (sum of Brönsted and Lewis acid sites) and DMPy (Brönsted sites) as probe molecules [29]. Very small volumes of solutes were injected to approach the conditions of gas chromatography linearity.

The experimental procedure used for temperature-programmed desorption of pyridine (Py-TPD) has already been described [30]. The apparatus used for Py adsorption/desorption was basically a gas chromatograph. This was modified with an empty column, placed before the catalyst tube and connected directly to the detector, so that the eluted band was recorded directly and peak retardation occurred only on the catalyst. The catalyst tube was made of 100 mm × 4 mm s.s. tube containing about 50 mg of catalyst packed between quartz wool plugs. Pure N_2 at a flow rate of 50 ml min^{-1} was used as the carrier gas. Before adsorption experiments were started, we pretreated the catalyst in situ by passing pure N_2 at a flow rate of 50 ml min^{-1} and heating the catalyst from 323 to 723 K at 10 K min^{-1}; the temperature was maintained at 723 K for 10 min. After catalyst pretreatment, the temperature was lowered to 373 K, at which point the adsorption experiment was carried out. Py-TPD experiments were performed in the 323–973 K range after saturation of the sample, followed by purging in N_2 at 373 K for 1 h. Desorption was measured with a flame ionization detector (FID).

Temperature-programmed desorption of pyridine–mass spectrometry (Py-TPD/MS) experiments were carried out in the on-line device described in section 2.2 for TP-MS experiments. The same Py-TPD experimental conditions were used.

2.4. Catalytic testing

Catalytic testing of cumene cracking was performed with a tubular stainless-steel, continuous-flow mixed-bed microreactor (6 mm i.d.) surrounded by an electric heater. An iron-constantan thermocouple was placed in the middle of the catalyst bed, and the unit was operated at atmospheric

pressure. The substrate was delivered at a set flow rate with a Gilson 307 Piston-Pump system and was vaporized before it was passed through the catalyst bed in the presence of a flow of nitrogen carrier gas (3 L h^{-1}). The catalyst charges (W) were small, usually ca. 0.1 g. These were held by quartz wool at almost the center of the reactor; the reaction temperature was 673 K. Standard catalyst pretreatment was carried out in situ at 673 K for 1 h under a stream of high-purity nitrogen before the reaction. To prevent any condensation of reactants or products, all connections were heated at 490 K. Blank runs at 673 K showed that under the experimental conditions used in this study, thermal effects could be negligible. The reaction products, characterized by gas chromatography–mass spectrometry, were propene and benzene and small amounts of α-methylstyrene.

3. Results and discussion

3.1. XRD experiments

Powder XRD patterns of the resultant materials obtained with CTMABr/OH 50% ion exchanged after calcination are shown in Fig. 1. The XRD patterns for samples XAl-50 and XAl-50-F with X = 40–20 showed diffraction peaks (211) and (200) similar to the characteristic diffraction pattern of the cubic member of the M41S family, MCM-48 [31,32]. HREM confirmed the identity of the samples (see below). Furthermore, the value of the ratio d_{220}/d_{211} obtained, ranging from 0.85 to 0.90, has been described as characteristic of cubic symmetry [12,25]. However, for materials obtained with CTMABr/OH 40% ion exchanged, we found that the predominant product was the hexagonal phase MCM-41 (Table 1). So for these series exclusively 40Al-40 and 40Al-40-F samples showed MCM-48 structure. These results suggest that both the degree of the hydroxide for bromide ion exchange and the Si/Al molar ratio in the synthesis gel determined the final mesostructure in our synthesis procedure.

The intensity of the XRD patterns increased for XAl-Y-F, with respect to XAl-Y samples, indicating an increase in the structural order of the cubic or hexagonal network with the NH_4F post-synthesis treatment, according to results previously reported for Si-MCM-41 [33] and Si-MCM-48 [5] when NaF was used. Moreover, the d_{211} line is used to calculate the unit cell parameter $a_0 = d\{h\,k\,l\}(h^2 + k^2 + l^2)^{1/2}$. All cubic XAl-Y and XAl-Y-F samples showed similar cubic unit cell parameters ranging from ca. 77 to ca. 87. The pore wall thickness was calculated according to the formula $\varepsilon = (a_0/3.092) - (D_{BJH}/2)$ [34]. Likewise, the unit cell expands with the NH_4F post-synthesis treatment for Al-MCM-48, whereas it remained almost unchanged for Al-MCM-41 materials (Table 1).

On the other hand, Nur et al. [35] have demonstrated that, in a mixture of hexagonal-cubic phases, the presence of MCM-48 at a certain level could not be identified by XRD because of very weak reflections. However, complementary

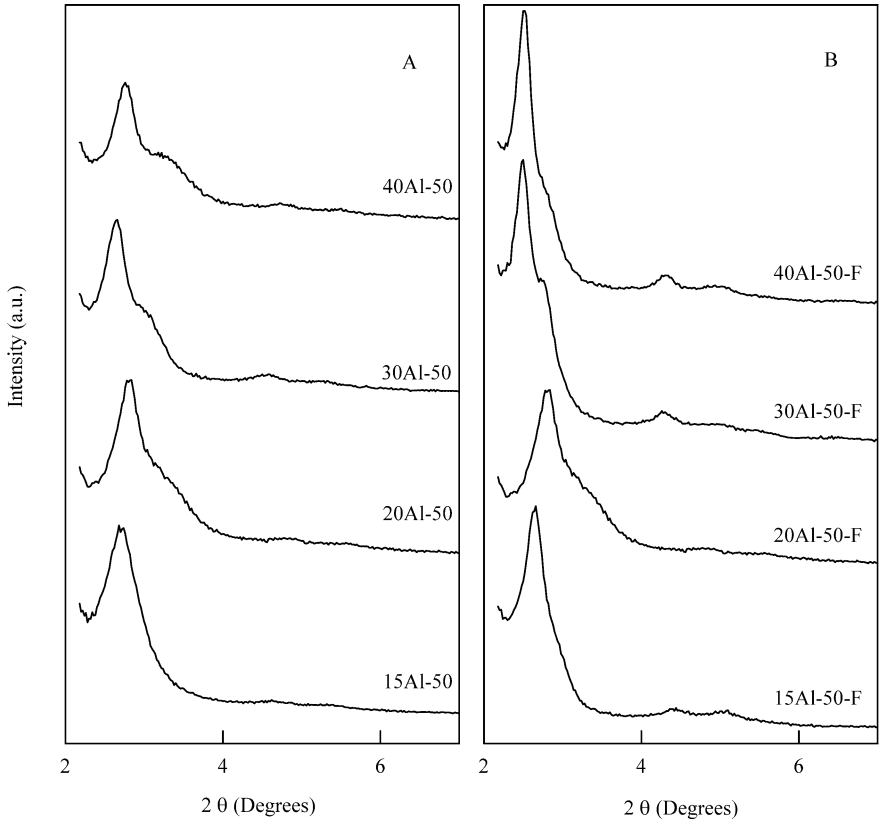

Fig. 1. XRD patterns of (A) XAl-50 and (B) XAl-50-F samples.

HREM studies demonstrated the absence of local MCM-48 mesophase in our MCM-41 materials.

3.2. Surface and textural properties

The isotherms were of type IV, corresponding to mesoporous solids (Fig. 2). As the relative pressure increased ($p/p_0 > 0.2$), the isotherms exhibited sharp inflections characteristic of capillary condensation within mesopores, which occurred at $p/p_0 = 0.2$ and 0.35. In any case, the sharpness of this step suggested an uniform size pore system and provided evidence of the high quality of the samples. Furthermore, a change was noticed between curves found for fluorinated samples and those for nonfluorinated samples, as depicted in Fig. 2. First of all, the slope of the adsorption isotherm in the 0.35 to 0.8 partial pressure region for XAl-Y-F samples was comparatively greater than that for XAl-Y samples. This indicated that the particle size and particle aggregation probably differed between the two batches of samples [36]. Thus the change in the hysteresis loop in the 0.35 to 0.6 partial pressure region was associated with framework mesoporosity, whereas the hysteresis loop at high partial pressure ($p/p_0 > 0.8$) was indicative of textural mesoporosity and/or macroporosity. Therefore, the absence of a loop for nonfluorinated samples suggested that these materials possessed pores in the lower mesopore range [37,38], whereas the sharp increase in nitrogen uptake at high pressure ($p/p_0 > 0.9$) in both batches of samples was indicative of a significant amount of interparticle mesoporosity.

Pore size distributions (PSDs) were obtained from the adsorption data by means of the Barret–Joyner–Halenda (BJH) method. The cumulative pore volume (V_{BJH}) was calculated in the width range of 15–400 Å. The BET surface area (S_{BET}), mesopore diameter (D_{BJH}), and cumulative pore volume (V_{BJH}) of aluminosilicate M41S samples are summarized in Table 1. Note that the Al-MCM-48 obtained by direct synthesis possesses a lower unit cell parameter and pore diameter than Al-MCM-48 obtained by NH_4F post-synthesis treatment. Consequently, the wall thicknesses of all Al-MCM-48 samples were similar (ca. 16 Å). So, in contrast to the effect of NaF post-synthesis treatment described for Si-MCM-41 and Si-MCM-48 [5,33], NH_4F could not be expected to improve the hydrothermal stability of our Al-MCM-48 samples.

3.3. SEM and HREM experiments

Scanning electron microscopy images in Fig. 3 show nonagglomerated particles, and, as can be expected from the synthesis procedure used, the particle morphology was spherical for all XAl-Y and XAl-Y-F materials, according to

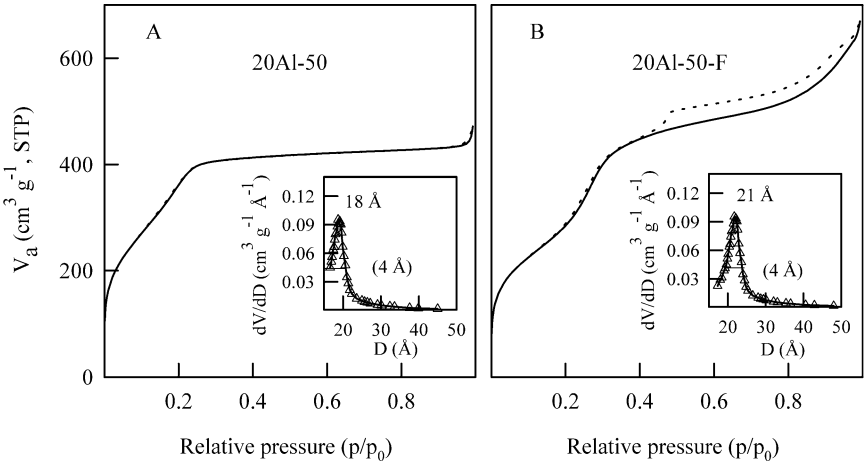

Fig. 2. Nitrogen adsorption–desorption isotherms and pore size distributions of (A) 20Al-50 and (B) 20Al-50-F samples.

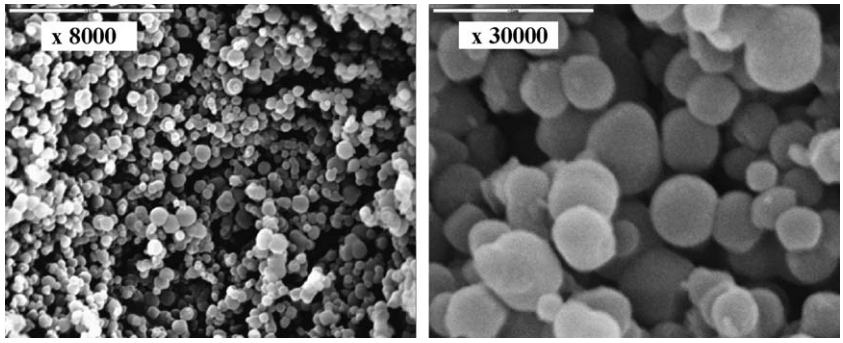

Fig. 3. SEM micrographs of 40Al-40 sample at different resolutions.

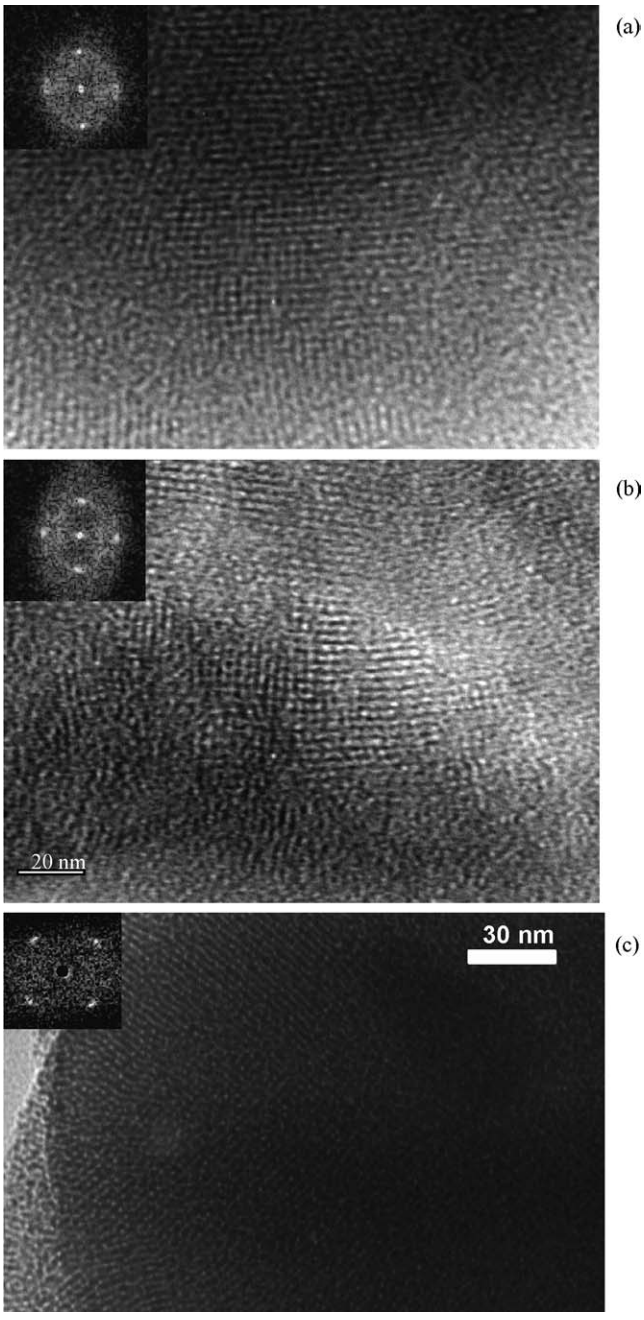

Fig. 4. HREM images of 40Al-50 sample. (a) and (b) on the ultramicrotomized and (c) powdered specimen.

the results of Grün et al. for mesoporous MCM-41 [27] and MCM-48 [17] materials. Thus NH_4F treatment did not affect the particle morphology of Al-MCM-48 samples.

Fig. 4 shows HREM images that are representative of the 40Al-50 sample. The first two, (a) and (b), were recorded on the ultramicrotomized specimen; (c) was obtained directly from the powdered specimen.

The spatial distribution of the pore structure, in projection, is clearly revealed in these images. Digital diffraction patterns obtained on selected regions, shown as insets, indicate in all cases a square pattern of dots, which is characteristic of the [1 0 0] projection of MCM-48. The diffraction spots in these DDPs correspond to a 2.8-nm distance. According to these results, the sample would present a local MCM-48 structure.

3.4. Thermogravimetric and differential thermal analysis results

The results of thermogravimetric (ATG) analysis and differential thermal analysis (DTA) of the 30Al-50-F and 30Al-50 samples are shown in Figs. 5A and B, respectively. Furthermore, all Al-M41S samples showed similar results in ATG-DTA analysis [12,39]. Four steps can be observed in Fig. 5. The first step, centered at ca. 368 K, is associated with physically adsorbed water, constituting about 5% weight loss. The second part of the ATG curve, at ca. 438–573 K, reflects thermal removal of the template, contributes to ca. 23% weight loss, and is attributed to the release of CTMABr in two ways: (i) desorption and decomposition (Hoffmann elimination reaction), corroborated by an endothermic peak in DTA centered at ca. 523 K, and bands at ca. 450–587 K in the TP-MS spectrum for 1-hexadecene and trimethylamine profiles (Fig. 5C); and (ii) oxidation (peak at ca. 526 K in the TP-MS spectrum for H_2O and CO_2 profiles, Fig. 5C). The third part, at 573–673 K, is attributed to the decomposition and oxidation of the remaining template, as confirmed by the TP-MS experiment and an exothermic effect in the DTA curve (ca. 9% weigh loss). The step in the ATG curve at 673–973 K may be attributed to the combustion of the remaining carbon species and water loss due to dehydroxylation of SiOH groups. Again, these results were confirmed by TP-MS spectra (Fig. 5C).

Temperature-programmed MS spectra consisting of the m/z signals 18 (H_2O), 43 (1-hexadecene), 44 (CO_2), and 58 (trimethylamine) of as-synthesized catalysts were obtained to corroborate the information about the thermal treatment of the Al-M41S catalysts (Fig. 5C).

3.5. ^{27}Al and ^{29}Si MAS NMR experiments

In very good agreement with ^{29}Si MAS NMR reported in the literature for Al-M41S materials [15], the ^{29}Si MAS NMR spectra for Al-MCM-48 samples here obtained were also very broad, so that the peak corresponding to Si(nAl) units were poorly resolved and deconvolution was further complicated by the presence of a peak at ca. −102 ppm [(Si(SiO)$_3$OH units] [15], regardless of the synthesis procedure. However, it was clear that the peak at ca. −110 ppm from Si(SiO)$_4$ and/or Si(OSi)$_3$OAl units (Q^4) sites [40] increased its relative intensity in the fluorinated samples, denoting an increase in the number of Q^4 sites (Fig. 6).

^{27}Al MAS NMR spectra for the hydrated calcined XAl-Y samples (Fig. 7) gave a resonance from four coordinate Al at ca. 53 ppm, indicating that the Al is incorporated into the framework. However, the ^{27}Al MAS NMR spectra for XAl-Y-F samples were different, exhibiting a low-intensity line at

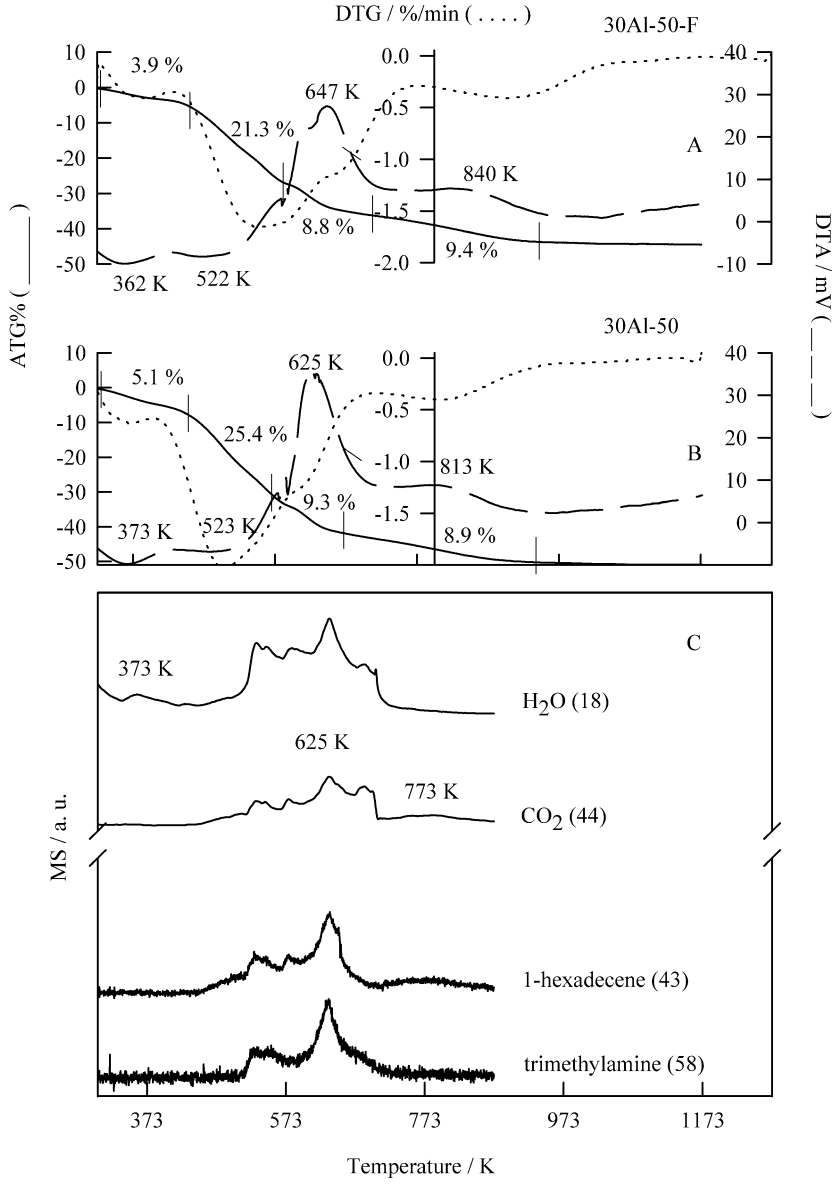

Fig. 5. ATG-DTA profiles of as-made (A) 30Al-50-F and (B) 30Al-50 samples, and TP-MS spectra of as-made (C) 30Al-50 sample.

ca. 53 ppm from four-coordinate aluminum (Al_t) and an intense line at ca. 0 ppm from six-coordinated aluminum (Al_o). These results imply aluminum extraction from the mesoporous aluminosilicate network in our MCM-48 materials during the NH_4F treatment in the synthesis procedure (ii). These results are in good agreement with those described by Xu et al. [26] for Al-MCM-41 materials.

3.6. Diffuse reflectance infrared Fourier transform measurements

The diffuse reflectance infrared Fourier transform (DRIFT) spectra of the as-synthesized and calcined Al-MCM-48 samples showed typical infrared absorption bands of the CTMABr and of M41S materials, respectively (Fig. 8) [14,15].

In the hydroxyl stretching vibration region (4000–2500 cm^{-1}), the hydroxyl groups associated with extraframework aluminum species (band at ca. 3690 cm^{-1}) for as-synthesized samples are noteworthy [41]. In addition to this, the band at 3693 cm^{-1} shifted to 3680 cm^{-1} when the samples were treated with NH_4F (Figs. 8a and b). This suggests that the nature of the Al environment changed during treatment with NH_4F. The absorption bands at 1036 and 1171 cm^{-1} were due to the asymmetrical stretching vibrations of Si–O–Si bridges.

Calcined Al-MCM-48 samples showed a sharp band at 3737 cm^{-1} arising from isolated Si–OH groups and a broad band at ca. 3500 cm^{-1} assigned to water and/or bridged hydroxyl groups (Figs. 8c and d). However, there was no infrared band in the spectra that could be attributed to isolated Al(OH) aluminum species. The DRIFT spectra in the

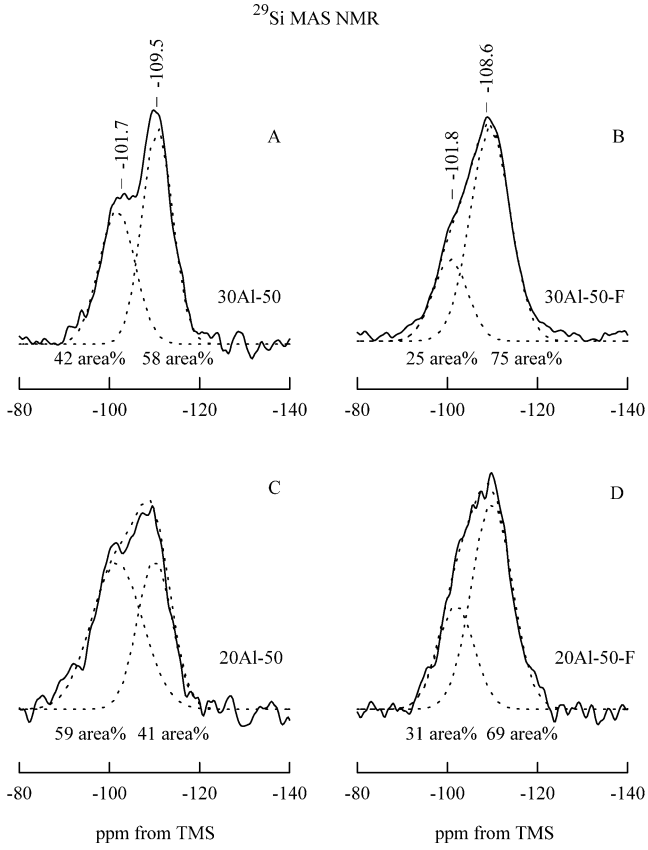

Fig. 6. ^{29}Si MAS NMR spectra of (A) 30Al-50, (B) 30Al-50-F, (C) 20Al-50 (D) 20Al-50-F samples.

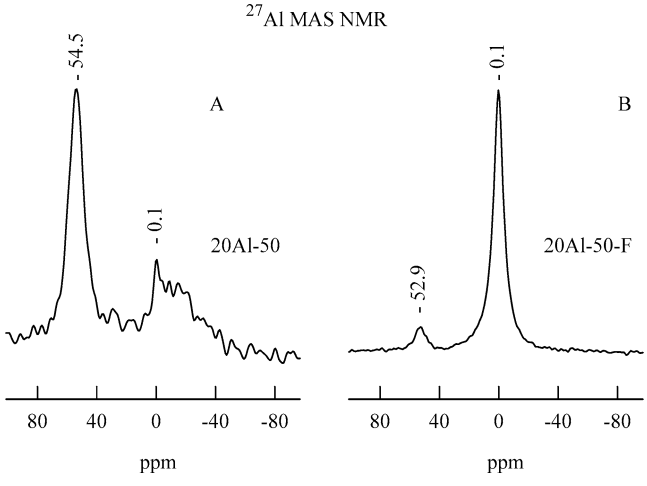

Fig. 7. ^{27}Al MAS NMR spectra of (A) 20Al-50 and (B) 20Al-50-F samples.

2500–400 cm^{-1} region contained bands at ca. 1036 and 1171 cm^{-1} (asymmetrical) and 803 cm^{-1} (symmetrical), due to Si–O stretching typical of M41S materials (Figs. 8c and d) [14,15].

3.7. Acid properties

Py and DMPy adsorption at 573 K was used to measure the Lewis and Brönsted acid sites on M41S materials, assuming that DMPy is selectively adsorbed on Brönsted acid sites and Py is adsorbed on both Brönsted and Lewis acid sites [42].

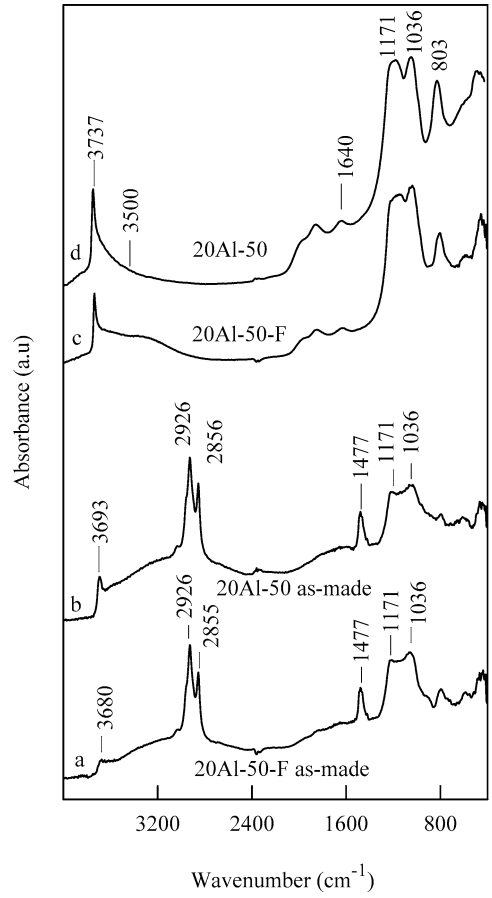

Fig. 8. DRIFT spectra of (a) as-made 20Al-50-F, (b) as-made 20Al-50, (c) 20Al-50-F, and (d) 20Al-50 samples, measured at 373 K against KBr reference.

Fluorinated M41S catalysts clearly increased Brönsted acidity compared with nonfluorinated catalysts, whereas Lewis acidity (difference between Py and DMPy adsorption) remained almost unchanged (Table 2). These results were similar to those reported by our group [42] for amorphous $AlPO_4$–Al_2O_3 catalysts and by Rodriguez et al. [43] for Al_2O_3 and were related to the F^- ion substitution for both Al–OH and P–OH hydroxyl groups and Al–OH groups, respectively. Likewise, Xu et al. [26] modified Al-MCM-41 with ammonium fluoride, and they demonstrated the formation of Si–F and extraframework Al(O_5F) species. In this way, when the F^- ion is substituted for both Al–OH and Si–OH groups in the Al-MCM-48 sample, the number of Brönsted acid sites decreases. So, the increase in Brönsted acidity has to be understood as an increase in the strength of the remaining OH groups.

On the other hand, a great increase in the total acidity of samples obtained with the use of CTMABr/OH (XAl-Y) is noticeable with respect to that obtained with CTMABr (Al-41-30) as the template. Finally, as can be expected, the total

Table 2
Surface acid density and contributions to the total area for Py-TPD profiles of Al-M41S and commercial zeolites catalysts

Catalyst	Titration at 573 K		Py-TPD (area %)			
	Py (μmol m^{-2})	DMPy (μmol m^{-2})	~ 460 K	~ 550 K	~ 700 K	~ 930 K
40Al-50	0.09	0.05	56	14	19	11
30Al-50	0.16	0.11	36	16	31	17
20Al-50	0.17	0.07	42	14	26	18
15Al-50	0.18	0.06	20	16	47	17
40Al-50-F	0.14	0.10	58	14	16	12
30Al-50-F	0.19	0.11	45	8	29	18
20Al-50-F	0.23	0.12	39	10	32	19
15Al-50-F	0.30	0.21	26	12	41	22
40Al-40	0.13	0.03	57	5	22	16
30Al-40	0.14	0.06	61	8	18	12
20Al-40	0.11	0.04	47	7	29	17
15Al-40	0.17	0.04	32	10	41	17
40Al-40-F	0.12	0.07	35	9	34	23
30Al-40-F	0.17	0.09	42	8	30	20
20Al-40-F	0.19	0.10	31	14	35	20
15Al-40-F	0.23	0.10	22	10	49	19
Al-41-30	0.11	–	19	36	31	14
ZSM5-30	–	–	14	20	47	19
HY-5.2	0.49	–	22	18	38	22

acidity increased as the aluminum content increased for all of our M41S samples (Table 2).

Figs. 9 and 10 show the DRIFT spectra for the Py adsorbed on XAl-50 and XAl-50-F samples, in the region of 1700–1400 cm^{-1}, subjected to different thermal treatments in the range 373–423 K. All aluminosilicate M41S catalysts exhibited several peaks due to Lewis-bonded Py (1618 and 1453 cm^{-1}) and Py bonded on Brönsted acid sites (1640 and 1543 cm^{-1}) and a band at 1492 cm^{-1} attributed to Py associated with both Lewis and Brönsted acid sites [42].

Furthermore, the spectra for adsorbed Py (Figs. 9 and 10) indicated an increased contribution of Brönsted acid sites in fluorinated M41S materials, confirming results obtained by the pulse chromatographic technique (see above). Moreover, the desorption of Py at increasing temperatures results in the removal of both Brönsted-bound and Lewis-bound Py.

Typical examples of Py-TPD results for Al-MCM-48 samples are shown in Fig. 11. The Py desorption trace was deconvoluted with the use of a Gaussian function, with temperature as a variant. Experimental data, the results of deconvolution and the theoretical spectrum obtained by summing the individual peaks (standard deviations $< 6\%$) of samples 20Al-50 and 20Al-50-F, are shown in Figs. 11A and B, respectively. Analogous spectra were obtained for all Al-MCM-48 and Al-MCM-41 samples. The first peak, around 460 K, was attributed to weak acid sites, and the Py peak at about 550 K was attributable to medium acid sites, whereas the next two peaks (around 700 and 930 K, respectively) were assumed to be due to strong acid sites (Brönsted and Lewis). As shown in Table 2, the peak centered at ca. 460 K decreased in contribution (area %), whereas the peak centered at ca. 700 K increased as the aluminum content increased for all Al-M41S catalysts. So, the total acidity became stronger as the aluminum content increased, regardless of the synthesis method. Moreover, TPD profiles acquired for H-Y and H-ZSM-5 zeolites were similar to those obtained for Al-M41S materials with Si/Al $\leqslant$ 20. On the other hand, acidity trends were also confirmed by the isopropylbenzene conversion test (see below).

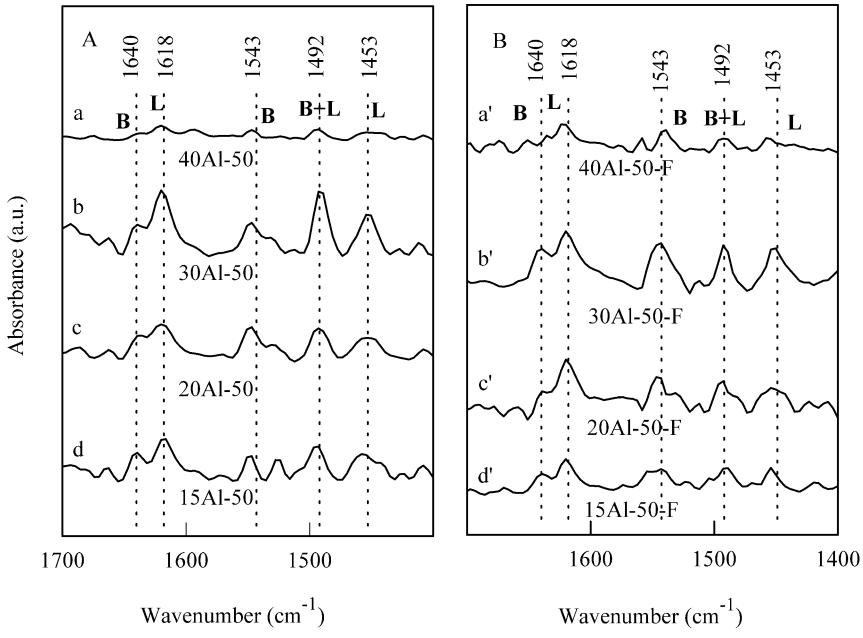

Fig. 9. DRIFT of adsorbed pyridine (1700–1400 cm^{-1}) over (A) XAl-50: (a) 40Al-50, (b) 30Al-50, (c) 20Al-50, and (d) 15Al-50; and (B) XAl-50-F: (a′) 40Al-50-F, (b′) 30Al-50-F, (c′) 20Al-50-F, and (d′) 15Al-50-F catalysts, which were treated at 423 K for 1 h under nitrogen, after adsorption of Py for 1 h and desorption at 373 K for another hour.

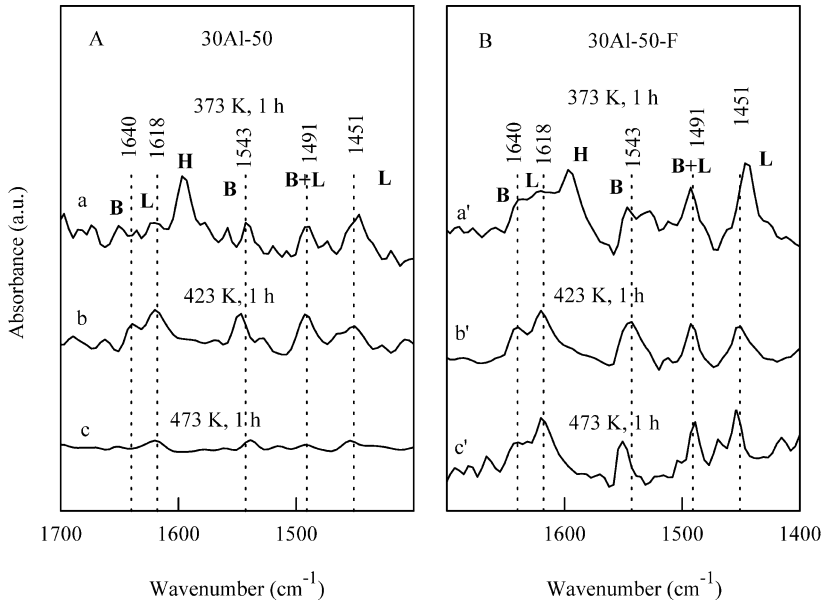

Fig. 10. DRIFT of adsorbed pyridine (1700–1400 cm^{-1}) of (A) 30Al-50 and (B) 30Al-50-F materials which were treated at 373 K under nitrogen, after adsorption of Py, for 1 h (a, a′). Then, the temperature was increased to 473 K and the catalyst remained, in the nitrogen stream, at 423 K additionally for 1 h (b, b′). Then, the temperature was increased to 473 K, the catalyst remaining at that temperature for 1 h (c, c′).

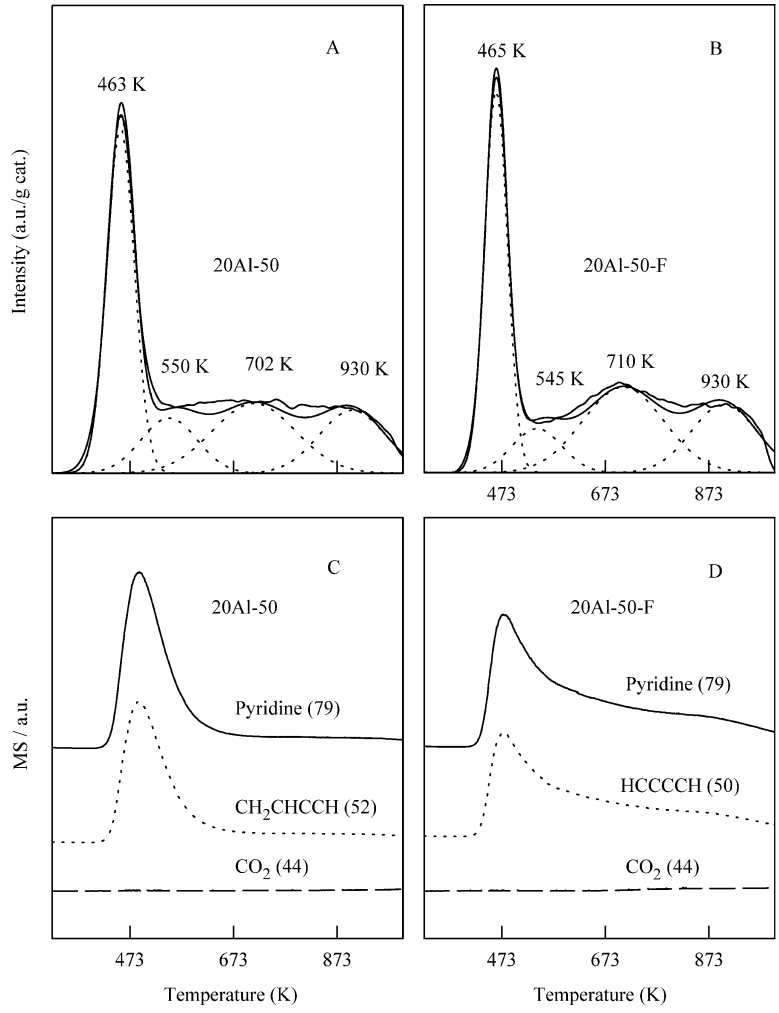

Fig. 11. Py-TPD profiles of (A) 20Al-50 and (B) 20Al-50-F and Py-TPD/MS spectra of (C) 20Al-50 and (D) 20Al-50-F materials.

The transformation of Py conversion to simpler compounds by cracking was excluded by Py-TPD/MS experiments (Figs. 11C and D). Thus, in Figs. 11C and D, ions 79 and 52, and 79 and 50, respectively, have a distorted intensity with a decreased relative intensity for ions 52 and 50 against 79. It can be concluded from this that the MS signal of these ions comes from an ion source of the MS spectrometer and in any case from Py cracking. Furthermore, we are aware of the retardation in Py desorption and different profile shapes in the Py-TPD/FID and Py-TPD/MS results. This arose from the capillary and bypass inlet system in the Py-TPD/MS experiment.

3.8. Catalytic activity experiments

In the absence of diffusion effects, cracking conversion data (X_T) are fitted to a first-order rate equation

$$\ln\left[1/(1-X_T)\right] = k(W/F),$$

where W is the catalyst weight and F is the feed rate. Calculations were performed only to compare the reactivities of the different catalysts and were not intended to determine the detailed rate equations. All values were reproducible to within about 8%. The initial reaction rate constants (k), X_T, and reaction selectivity for cracking (S_{CK}) are collected in Table 3.

Benzene and propene were always the main reaction products found in catalytic test reactions of isopropylbenzene conversion on our Al-M41S catalysts. As shown in Table 3, the degree of the surfactant hydroxyl exchange in the synthesis gel and/or NH_4F post-synthesis treatment did not exert a remarkable effect on activity and selectivity for cracking in isopropylbenzene conversion over these Al-M41S catalysts. However, those catalysts with Si/Al $\leqslant$ 20 showed the highest conversion levels for this reaction, which is in agreement with the acid strength for these samples.

On the other hand, the NH_4F treatment has led to an enhancement of Brönsted acid sites, when compared with Lewis sites (as can be seen from the acid properties of samples), and a change was also found in the aluminum environment due to the fluorination treatment (it is evident from ^{27}Al MAS NMR and DRIFT data that the nature of the acidity of XAl-Y is different from that of XAl-Y-F). This has recently been reported by our group for Al-MCM-41 synthesized in a similar way [39]. Indeed, rather than the total acidity, probably an acidity of a particular strength and type was responsible for isopropylbenzene conversion on Al-M41S catalysts.

However, the catalytic activity of XAl-Y-F may be attributed to extraframework aluminum species (possibly AlO_5F species), whereas for XAl-Y it should be ascribed to structural aluminum. Therefore, it is not very clear whether this fluoridation could be accompanied by an increase in the catalytic activity in the Al-MCM-48 samples, although a significant increase in catalytic activity has been reported when fluorination takes place [32]. Thus, the values shown in Table 3 could suggest that in terms of catalytic conversion level, XAl-Y and XAl-Y-F materials were close to commercial H-Y, although a greater catalytic conversion level was found in isopropylbenzene cracking for H-ZSM-5. When the commercial silica–alumina catalyst (Si235, 13 wt% Al_2O_3) and the aluminosilicate Al-41-30 synthesized by a different

Table 3
Isopropylbenzene conversion (X_T, mol%), reaction rate constant (k, mol g^{-1} s^{-1}), selectivity to cracking (S_{CK}, mol%) and deactivation rate ($D = X_{T(4\text{ h})} - X_{T(20\text{ h})}/X_{T(4\text{ h})} \times 100$) over Al-MCM-48 and commercial silica–alumina and zeolites catalysts[a]

Catalyst	4 h on stream			12 h on stream			20 h on stream			D
	X_T	$k \times 10^6$	S_{CK}[c]	X_T	$k \times 10^6$	S_{CK}	X_T	$k \times 10^6$	S_{CK}	(%)
40Al-50	17.6	21.1	98.4	15.1	18.0	98.5	13.4	16.0	98.8	24
30Al-50	12.6	14.7	97.8	9.6	11.4	98.2	8.4	10.0	98.1	33
20Al-50	23.9	28.5	100.0	19.7	23.5	99.5	18.0	21.5	99.4	25
15Al-50	23.8	28.4	98.7	19.4	23.2	98.8	16.6	19.8	99.4	30
40Al-50-F	12.7	15.2	96.0	10.5	12.5	97.1	9.6	11.5	97.3	24
30Al-50-F	18.6	22.2	99.5	15.1	18.0	99.5	13.6	16.1	99.5	27
20Al-50-F	23.7	28.2	98.3	19.6	23.4	100.0	17.9	21.3	100.0	24
20Al-50-F[b]	45.0	53.8	99.6	35.6	42.5	99.5	32.2	38.5	99.3	28
15Al-50-F	18.9	22.5	99.3	14.9	19.3	99.4	13.4	15.9	99.6	29
40Al-40	13.5	16.1	98.1	11.9	14.2	98.1	11.4	13.7	98.6	16
30Al-40	15.2	18.1	98.9	14.7	17.5	98.6	12.7	15.2	99.0	16
20Al-40	13.9	16.6	98.4	11.0	13.1	98.1	10.0	12.0	98.5	28
15Al-40	14.0	16.7	98.1	13.1	15.6	98.2	11.6	13.8	98.6	17
40Al-40-F	9.3	11.1	100.0	8.4	10.0	100.0	6.0	7.2	100.0	35
30Al-40-F	9.3	11.1	100.0	7.8	9.4	98.7	7.5	9.0	98.7	19
20Al-40-F	17.8	21.1	99.7	14.5	17.3	98.3	13.0	15.5	98.3	27
15Al-40-F	22.9	27.3	98.8	20.2	24.1	98.8	18.1	21.6	100.0	21
Al-41-30	10.3	12.4	98.7	8.3	9.9	98.5	6.6	8.1	98.2	36
Si235	8.6	10.2	91.4	6.4	7.6	90.7	4.1	5.0	87.5	52
HY-5.2	19.2	22.9	95.7	13.0	15.5	95.2	10.5	13.2	94.0	45
ZSM5-30	40.0	61.0	98.3	32.4	46.8	98.6	25.4	35.0	97.3	37

[a] $T = 673$ K.
[b] $T = 723$ K, $F = 1.19 \times 10^{-5}$ mol s^{-1}, WHSV = 51.7 h^{-1}.
[c] Difference to 100 mol% corresponds to α-methylstyrene.

procedure were compared, XAl-Y and XAl-Y-F catalysts showed better catalytic activity. In any case, selectivities for cracking remained almost constant for the whole process. Finally, a slight deactivation was noticed along with time on stream (25–30% after 16 h) for both batches of samples, whereas a stronger deactivation (40–50%) was found for Al-41-30 and commercial H-Y, H-ZSM-5 (at a similar conversion level, sample 20Al-50-F at 723 K), and Si235 catalysts.

4. Conclusions

Variables in the synthesis procedure, such as the Si/Al ratio and degree of the surfactant hydroxyl exchange, were critical for obtaining the MCM-48 structure instead of MCM-41. Nonfluorinated and fluorinated Al-M41S materials were strong acid catalysts. The post-treatment in NH_4F solution led to Al-MCM-48 with an improved degree of ordering and analogous general acid properties, although it promoted an enhancement of Brönsted acidity. However, the local structure of extraframework aluminum in fluorinated samples was of octahedrally coordinated aluminum (probably due to AlO_5F species), implying that this new aluminum was in fact responsible for the acidity and the catalytic activity in the isopropylbenzene cracking reaction of these fluorinated materials, whereas, in nonfluorinated samples, this could be attributed to tetrahedral framework aluminum.

Al-M41S catalysts showed remarkably high activity in the isopropylbenzene cracking reaction, higher than that of the Al-41-30 sample, commercial H-Y zeolite, and Si235 catalysts. Furthermore, our samples suffered lower deactivation with time on stream than the Al-41-30 sample, commercial H-Y, ZSM-5 zeolites, and Si235 catalysts.

Acknowledgments

The financial support received from the Direccion General de Investigacion (Project BQU2001-2605), Ministerio de Ciencia y Tecnologia, FEDER funds, and from the Consejeria de Educacion y Ciencia (Junta de Andalucia) is gratefully acknowledged. We thank Professor M. Sullivan for linguistic revision of the manuscript.

References

[1] O.J. Sjöblom, M. Stöcker, Adv. Colloid Interface Sci. 89–90 (2001) 439.
[2] S. Jun, J.M. Kim, R. Ryoo, Y.-S. Ahn, M.-H. Han, Micropor. Mesopor. Mater. 41 (2000) 119.
[3] Q.-H. Xia, K. Hidajat, S. Kawi, Chem. Lett. (2001) 654.
[4] J.-H. Sun, M.-O. Coppens, J. Mater. Chem. 12 (2002) 3016.
[5] W.J. Kim, J.C. Yoo, D.T. Hayhurst, Micropor. Mesopor. Mater. 49 (2001) 125.
[6] W. Zhao, Q. Li, Chem. Mater. 15 (2003) 4160.
[7] N. Igarashi, K.A. Koyano, Y. Tanaka, S. Nakata, K. Hashimoto, T. Tatsumi, Micropor. Mesopor. Mater. 59 (2003) 43.
[8] Y. Xia, R. Mokaya, J. Phys. Chem. 107 (2003) 6954.
[9] A. Doyle, B.K. Hodnett, Micropor. Mesopor. Mater. 63 (2003) 53.
[10] Y. Xia, R. Mokaya, Micropor. Mesopor. Mater. 68 (2004) 1.
[11] H. Landmesser, H. Kosslick, U. Kürschmer, R. Fricke, J. Chem. Soc., Faraday Trans. 94 (1998) 971.
[12] H. Kosslick, G. Lischke, H. Landmesser, B. Parlitz, W. Storek, R. Fricke, J. Catal. 176 (1998) 102.
[13] S.E. Dapurkar, P. Selvam, Appl. Catal. A 254 (2003) 239.
[14] A.A. Romero, M.D. Alba, W. Zhou, J. Klinowski, J. Phys. Chem. B 101 (1997) 5294.
[15] A.A. Romero, M.D. Alba, J. Klinowski, J. Phys. Chem. B 102 (1998) 123.
[16] F. Chen, F. Song, Q. Li, Micropor. Mesopor. Mater. 29 (1999) 305.
[17] K. Schumacher, M. Grün, K.K. Unger, Micropor. Mesopor. Mater. 27 (1999) 201.
[18] W. Zhao, J. Yao, X. Huang, Q. Li, Chinese Sci. Bull. 46 (2001) 1436.
[19] M.L. Peña, Q. Kan, A. Corma, F. Rey, Micropor. Mesopor. Mater. 44–45 (2001) 9.
[20] S. Wang, D. Wu, Y. Sun, B. Zhong, Mater. Res. Bull. 36 (2001) 1717.
[21] D. Kumar, K. Schumacher, C. du Fresne von Hohenesche, M. Grün, K.K. Unger, Colloid Surf. A 187–188 (2001) 109.
[22] O. Collart, P. Van Der Voort, E.F. Vansant, D. Desplantier, A. Galarneau, F. Di Renzo, F. Fajula, J. Phys. Chem. B 105 (2001) 12771.
[23] G.A. Eimer, L.B. Pierella, G.A. Monti, O.A. Anunziata, Catal. Lett. 78 (2002) 1.
[24] Y. Xia, R. Mokaya, J. Mater. Chem. 13 (2003) 657.
[25] Ch. Danumah, S. Vauderuil, L. Bonneviot, M. Bousmina, S. Giasson, S. Kaliaguine, Micropor. Mesopor. Mater. 44–45 (2001) 241.
[26] M. Xu, W. Wang, M. Seiler, A. Buchholz, M. Hunger, J. Phys. Chem. B 106 (2002) 3202.
[27] M. Grün, K.K. Unger, A. Matsumoto, K. Tsutsumi, Micropor. Mesopor. Mater. 27 (1999) 207.
[28] E.P. Barret, L.G. Joyner, P.P. Halenda, J. Am. Chem. Soc. 73 (1951) 373.
[29] J.M. Campelo, A. Garcia, D. Luna, J.M. Marinas, J. Mater. Sci. 25 (1990) 2513.
[30] J.M. Campelo, A. Garcia, D. Luna, J.M. Marinas, A.A. Romero, Thermochim. Acta 261 (1995) 175.
[31] C.T. Kresge, M.E. Leonowicz, W.J. Roth, J.C. Vartuli, J.S. Beck, Nature 359 (1992) 710.
[32] J.S. Beck, J.C. Vartuli, W.J. Roth, M.E. Leonowicz, C.T. Kresge, K.D. Schmitt, C.T.W. Chu, D.H. Olson, E.W. Sheppard, S.B. McCullen, J.B. Higgins, J.L. Schlenker, J. Am. Chem. Soc. 114 (1992) 10834.
[33] W.J. Kim, J.C. Yoo, D.T. Hayhurst, Micropor. Mesopor. Mater. 39 (2000) 177.
[34] K. Schumacher, P.I. Ravikovitch, A. Du Chesne, A.V. Neimark, K.K. Unger, Langmuir 16 (2000) 4648.
[35] H. Nur, L.C. Guan, S. Endud, H. Hamdam, Mater. Lett. 58 (2004) 1971.
[36] S. Biz, M.G. White, J. Phys. Chem. B 103 (1999) 8432.
[37] P.T. Tanev, M. Chibwe, T.J. Pinnavaia, Nature 368 (1994) 321.
[38] J. Rathousky, A. Zukal, O. Franke, G. Shulzekloff, J. Chem. Soc. Faraday Trans. 90 (1994) 2821.
[39] J.M. Campelo, D. Luna, R. Luque, J.M. Marinas, A.A. Romero, in: 4th International Mesostructured Materials Symposium, Cape Town (South Africa), 2004, p. 309.
[40] W. Kolodziejski, A. Corma, M.T. Navarro, J. Perez-Pariente, Solid State Nucl. Magn. Reson. 2 (1993) 253.
[41] G. Catana, D. Baetens, T. Mommaerts, R.A. Schoonheydt, B.M. Weckhuysen, J. Phys. Chem. B 105 (2001) 4904.
[42] F.M. Bautista, J.M. Campelo, A. Garcia, D. Luna, J.M. Marinas, A.A. Romero, J.A. Navio, M. Macias, J. Catal. 145 (1994) 107.
[43] L.M. Rodriguez, J. Alcaraz, M. Hernandez, Y. Ben Taarit, M. Vrinat, Appl. Catal. A: Gen. 169 (1998) 15.